# High-Quality $CrO_2$ Nanowires for Dissipation-less Spintronics

Amrita Singh, Charlotte Jansen, Kaveh Lahabi, and Jan Aarts*
*Huygens-Kamerlingh Onnes Laboratory, Leiden University, P.O. Box 9504, 2300 RA Leiden, The Netherlands*
(Received 29 June 2016; published 18 October 2016)

Superconductor-ferromagnet (S-F) hybrids based on half-metallic ferromagnets, such as $CrO_2$, are ideal candidates for superconducting spintronic applications. This is primarily due to the fully spin-polarized nature of $CrO_2$, which produces enhanced long-range triplet proximity effects. However, reliable production of $CrO_2$-based Josephson junctions (JJs) has proved to be extremely challenging because of a poorly controlled interface transparency and an incomplete knowledge of the local magnetization of the $CrO_2$ films. To address these issues, we use a bottom-up approach to grow $CrO_2$ nanowires on prepatterned substrates via chemical-vapor deposition. A comprehensive study of the growth mechanism enables us to reliably synthesize faceted, homogeneous $CrO_2$ wires with a well-defined magnetization state. Combining these high-quality wires with a superconductor produces JJs with a high interface transparency, leading to exceptionally large 100% spin-polarized supercurrents, with critical current densities exceeding $10^9$ $Am^{-2}$ over distances as long as 600 nm. These $CrO_2$-nanowire-based JJs thus provide a realistic route to creating a scalable device platform for dissipation-less spintronics.

DOI: 10.1103/PhysRevX.6.041012 Subject Areas: Spintronics, Superconductivity

## I. INTRODUCTION

Ferromagnetic nanostructures have emerged as a leading candidate for spintronic applications because of their ability to carry spin-polarized currents [1,2]. However, one of the biggest challenges facing the field of spintronics is the large amount of dissipation that is generated by current-driven processes at the nanoscale [3,4]. One way to address this issue is to combine a ferromagnet (F) with a superconductor (S) to produce supercurrents in the ferromagnet. This method seems counterintuitive since electron spins in the Cooper pair are aligned antiparallel in a superconductor, while a ferromagnet prefers parallel spins. However, it has been shown that by engineering the S-F interface, supercurrents can indeed be injected into the ferromagnet [5–11]. The novelty of this induced supercurrent lies in its spin-polarized nature [12–14]. Such spin-polarized triplet Cooper pairs can only be generated when singlet Cooper pairs at the S-F interface are subjected to spin mixing and rotation [15], usually achieved by introducing an additional thin ferromagnetic layer at the interface [9,10,16,17]. Since triplet Cooper pairs are not affected by the exchange field of the ferromagnet, they can survive over considerably long distances, thereby giving rise to spin-polarized supercurrents.

Half-metallic ferromagnets are fully spin polarized and are expected to enhance the generation of triplet Cooper pairs [18], making them an ideal material choice for dissipation-less spintronics. This idea is indeed supported by experimental studies of $CrO_2$, a well-known half-metallic ferromagnet. S-F-S Josephson junctions fabricated on films of $CrO_2$ have been shown to carry large supercurrents [8]. Furthermore, the spatial extent of induced triplet correlations in $CrO_2$ is of the order of a micron [19,20], while it is limited to a few tens of nanometers for standard ferromagnets (Ni, Co, Fe). Finally, recent experiments in a spin-valve geometry [21,22] provide direct evidence that triplet generation is enhanced by more than an order of magnitude in $CrO_2$, as compared to other ferromagnets.

Despite the fact that $CrO_2$ clearly holds great promise for superconducting spintronics, progress in this field has been impeded because of a poorly controlled S-F interface transparency, ill-defined current paths, and an incomplete knowledge of the local magnetization state associated with full films of $CrO_2$. Here, we show that all of these problems can be circumvented by growing high-quality $CrO_2$ nanowires via selective area growth. We show that a thorough understanding of the growth process is vital for the generation of high-quality S-F-S JJs. By studying the effects of confinement, growth time, and crystal orientation on the magnetic and structural morphology of these structures, we demonstrate the reliable growth of homogeneous, crystalline nanowires with a desired geometry and magnetization state. This robust control over the magnetization and transparency enables us to reproducibly fabricate $CrO_2$-based JJs with record-high critical current

*aarts@physics.leidenuniv.nl

densities, and thus, it represents a crucial step towards the realization of a scalable superconducting spintronics device platform based on half-metallic ferromagnets.

It has been shown that full films of $CrO_2$ can be grown epitaxially via chemical-vapor deposition (CVD) [23,24]. One might imagine that the most convenient way to create $CrO_2$ structures with a well-defined geometry would be to follow a top-down approach by etching away selected portions of the full film. However, etching damages the edges of the structure. Furthermore, full-film growth results in the creation of a large number of grain boundaries, which remain present in the final device [see Fig. 1(f)] and are likely to reduce into insulating $Cr_2O_3$, thus suppressing current and supercurrent flow. It is therefore desirable to create these structures via a bottom-up approach such as selective area growth (SAG). SAG relies on the fact that $CrO_2$ is only known to grow epitaxially on $TiO_2$ or sapphire substrates. Thus, a patterned $SiO_x$ mask can be used to define the geometry of the $CrO_2$ nanostructures as shown in Fig. 1(a) (details of the growth are provided in the Methods section). The growth of $CrO_2$ nanowires proceeds through two important stages, as discussed below.

The initial stage of growth involves the nucleation and growth of $CrO_2$ inside the trench [see schematic in Fig. 1(a)]. A detailed understanding of this stage is essential to identify the parameters that affect the quality of the crystal. In order to probe this stage, the wires were grown for 20 min, which is just enough to fill the 25-nm-deep $SiO_x$ trench. Figures 1(b)–1(f) show the scanning electron microscopy (SEM) images of nanowires with trench width $w_{tr}$ varying from 230 nm to 2 $\mu$m. The L shape is chosen in order to compare the growth along different crystallographic axes. Along the (001) axis, we find that the growth is homogeneous for smaller trench widths (230 nm and 530 nm), but it becomes increasingly inhomogeneous for the wider trenches (1 $\mu$m and 2 $\mu$m). The explanation for this lies in the fact that the nucleation of $CrO_2$ occurs preferentially at the $SiO_x/TiO_2$ interface, followed by propagation of the growth front towards the center of the trench. This process is self-limited and is characterized by a length scale $\lambda$ bearing resemblance to a surface diffusion length. Therefore, if $w_{tr} < 2\lambda$, the growth is homogeneous [Figs. 2(b) and 2(c)], whereas for $w_{tr} > 2\lambda$ a void is formed at the center of the trench [Figs. 2(d) and 2(e)]. Growth along the (010) axis follows a similar mechanism for $w_{tr} > 2\lambda$, but for narrower trenches, we observe a different type of inhomogeneous filling, in which vertical growth along the wall is followed by inward lateral growth (see Ref. [25]). We note that our studies are quite different from earlier reports, where it was assumed that $CrO_2$ nucleates and grows uniformly in the narrow trenches away from the $SiO_x$ side walls [26].

As the growth time is increased, the $CrO_2$ begins to grow laterally above the $SiO_x$ mask [see Fig. 2(a)], accompanied by a significant change in its surface morphology. The most striking observation is the appearance of well-defined crystal facets, which (as will be shown later) provide an excellent interface for $CrO_2$-based JJs. Figures 2(b)–2(d) show the evolution of such facets with the growth time ($t_g$), upon deposition in disk-shaped trenches. For $t_g = 20$ min, growth is restricted to the (circular) trench, resulting in the formation of $CrO_2$ disks. With a further increase in $t_g$ (25 min), $CrO_2$ starts to overgrow laterally on $SiO_x$, and [011] facets begin to appear, presumably to minimize the total surface energy. For $t_g = 45$ min, the $CrO_2$ islands exhibit fully developed facets with smooth surfaces. This type of facet evolution with growth time has been reported recently for SAG of GaN [27].

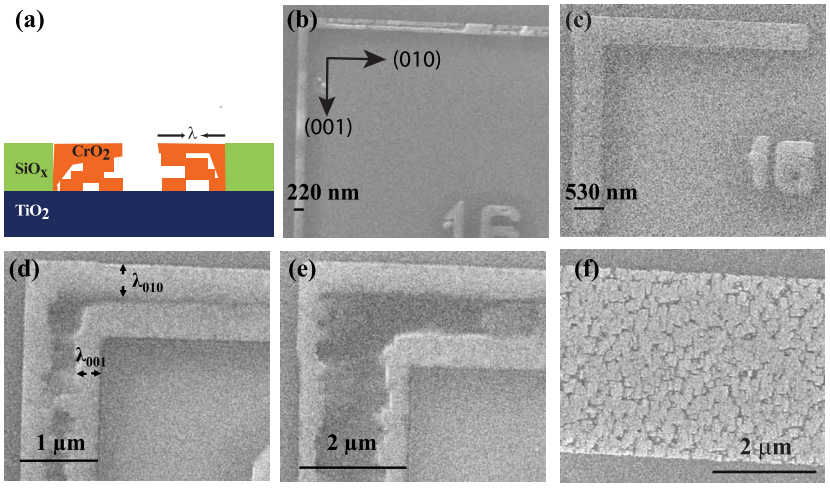


FIG. 1. Early stage growth of $CrO_2$ wires. (a) Schematic of edge-enhanced nucleation and growth of $CrO_2$ inside a $SiO_x$ trench. SEM of L-shaped nanowires along the indicated directions, grown for 20 minutes, with trench widths (b) 220 nm, (c) 530 nm, (d) 1 $\mu$m, and (e) 2 $\mu$m. The measured width of the $CrO_2$ bars is shown and found to be equal to the trench width. In panel (d), $\lambda$ is a measure for the surface diffusion length. (f) SEM image of $CrO_2$ wire fabricated via reactive ion etching of a $CrO_2$ film.

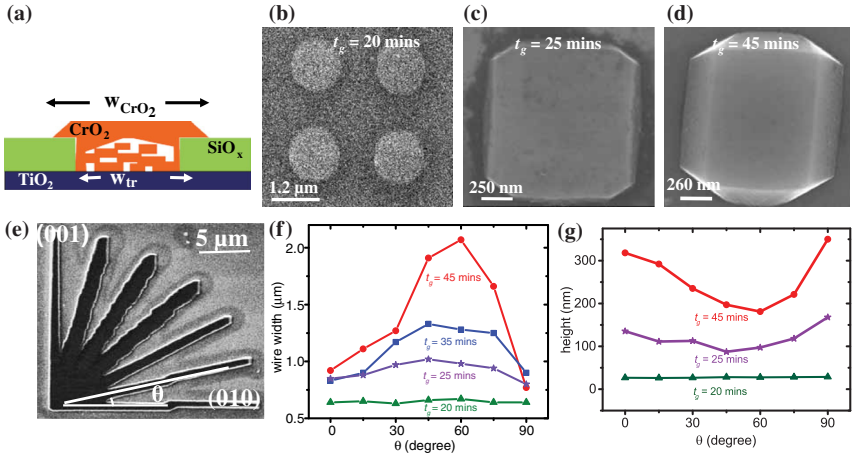


FIG. 2. Lateral overgrowth and facet evolution. (a) Schematic of lateral epitaxial overgrowth of $CrO_2$ over $SiO_x$ for higher growth times. Scanning electron micrographs of $CrO_2$ structures, all grown in circular $SiO_2$ trenches, for (b) 20 min (filling the disk-shaped trench), (c) 25 min, and (d) 45 min. The latter two are overgrowth structures. (e) Scanning electron micrographs of $CrO_2$ nanowires oriented between $\theta = 0°$ (010) and $\theta = 90°$ (001) at the intervals of 15° and grown in 500-nm-wide trenches for 45 min. Angular dependence of (f) width and (g) height of $CrO_2$ nanowires, grown in 500-nm-wide $SiO_x$ trenches, for different growth times.

In addition to the formation of crystalline facets, the extent of lateral overgrowth naturally determines the effective dimensions of the $CrO_2$ structures. We quantify this by studying the $CrO_2$ growth in $SiO_x$ trenches oriented along different crystallographic directions. Figure 2(e) shows a SEM image of $CrO_2$ wires grown in 500-nm-wide trenches for 45 min. It is clear that the extent of overgrowth depends strongly on orientation of the wire; however, it hardly depends on the trench width (see Fig. 2 of Ref. [25]). The anisotropy of lateral overgrowth with SAG has been reported earlier for thick $CrO_2$ structures [26,28]. However, from our data, we can extract quantitative information about the anisotropy, which is important for the accurate determination of critical current density in S-F-S JJs.

In Fig. 2(f), we plot the average wire width as a function of $\theta$ [angle relative to the (010) axis] for different $t_g$. The anisotropy is largest for $t_g = 45$ min and reduces with a decrease in $t_g$. The maximum lateral overgrowth occurs roughly at $\theta = 60°$, the direction which coincides with the diagonal of the $CrO_2$ unit cell. The height of the wires reaches a minimum at this angle, not unexpectedly, since lateral overgrowth occurs at the expense of vertical growth. This result is in contrast with the previous reports on SAG of $CrO_2$ structures where vertical overgrowth was reported to be isotropic [28]. This correlation between vertical and lateral growth can be understood on the basis of a mass transport mechanism and is explained in more detail in Ref. [25].

Our discussion thus far clearly shows that we can grow high-quality, homogeneous, and crystalline wires of $CrO_2$. The controlled growth of these wires along specific crystallographic directions allows us to exploit the shape anisotropy to reliably create specific magnetization states, a vital ingredient for the generation of triplet supercurrents. It is known that for $CrO_2$ films, the magnetic hard (easy) axis is aligned along the 010 (001) axis [26,29,30]. Figure 3(a) shows a magnetic force microscopy (MFM) image of $CrO_2$ wires grown along different crystallographic orientations. Away from the easy axis, striplike domains form in order to minimize the total magnetic energy. This is seen as alternating bright or dark contrast in the MFM image, and more clearly as oscillations in the magnetic phase contrast [Fig. 3(b) top and middle panels]. However, the wire oriented along (001) is in a single domain state, evident from the absence of contrast in the MFM image and the representative line scan along this direction

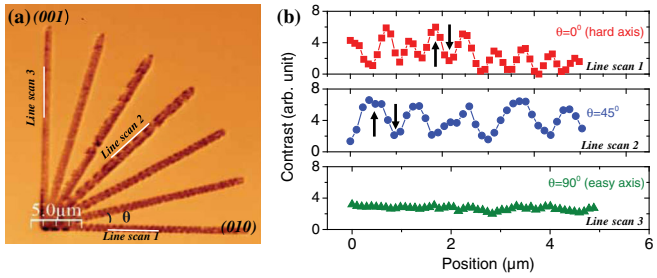


FIG. 3. Tuning magnetic domains by shape anisotropy. (a) Magnetic force micrograph of $CrO_2$ nanowires grown in 500-nm-wide trenches, oriented between $\theta = 0°$ and $\theta = 90°$ at intervals of 15°. White lines along the edges of the wires represent the line scan used to determine the magnetic phase contrast. Prior to MFM measurements, the samples were first magnetized with a 1-T field along the easy axis, followed by setting the field to −8 mT along the same axis. (b) Magnetic phase contrast along the edges of the wires for $\theta = 0°$ (upper panel), $\theta = 45°$ (middle panel), and $\theta = 90°$ (lower panel). Up and down arrows represent the opposite orientation (180°) domains.

[Fig. 3(b) bottom panel]. We use these high-quality $CrO_2$ wires grown along the easy axis to create S-F-S JJs. It is important to stress here that such local control over the magnetization is impossible to achieve in full films (see Fig. 3 of Ref. [25]), reflecting directly in a larger spread in performance of JJ devices.

While the crystalline facets of our $CrO_2$ wires grown via SAG provide transparent S-F interfaces, the uniform magnetization of the wire enables us to reliably engineer the magnetic inhomogeneity at the interface. This is achieved through the deposition of a Ni wire (mixer layer). The shape anisotropy of the Ni layer is such that its magnetization is perpendicular to the $CrO_2$ wire [see schematic in Fig. 4(a)]. This ensures the maximum possible magnetic noncollinearity at the S-F interface, resulting in efficient triplet Cooper pair generation. The mixer layer is part of a trilayer contact consisting of Cu (or Ag), Ni, and the superconductor (amorphous MoGe) (see Methods section for fabrication details). The Cu (or Ag) prevents exchange coupling between $CrO_2$ and Ni, while MoGe induces the proximity effect. Figure 4(a) shows a SEM image (false color) of a JJ device. We present results from two JJs (J1 and J2) whose device parameters are summarized in Table 1.

Figure 4(b) shows a plot of resistance ($R$) vs temperature ($T$) for J1 measured in quasi-4 probe geometry. Around $T = 6.5$ K, $R$ drops sharply because of the superconducting transition in the MoGe leads. Cooling further (below 5 K), the JJ reaches a zero resistance state [inset Fig. 4(b)] accompanied by the appearance of a supercurrent. The measured resistance of the device is dominated by the Cu layer in the leads since the Cu specific resistivity $\rho_{0,Cu}$ of the order of 5 $\mu\Omega$ cm is much smaller than $\rho_{0,MoGe} \approx 200\ \mu\Omega$ cm. Taking a length of 70 $\mu$m per lead, a width of 2.5 $\mu$m, and a thickness of 5 nm, we find 560 Ω. The normal resistance of the $CrO_2$ weak link we estimate using $\rho_{0,CrO_2} \approx 6\ \mu\Omega$ cm (along the easy axis) to be 0.32 Ω. This leaves about 20 Ω as the contact resistance. We note in Fig. 4(b) that the low-temperature R is well below 0.32 Ω. Figure 4(c) shows $I$-$V$ characteristics of J1 at a few different temperatures and is used to extract the critical current. The voltage increase just above $I_c$ starts with a small steep slope, but then it settles to a slope that is close to 0.3 Ω, quite as expected for the $CrO_2$ weak link. The value of $I_c$, along with a precise knowledge of the dimensions of $CrO_2$ wires, allows us, for the first time, to reliably estimate the critical current density ($J_c$) of $CrO_2$-based JJs. In Fig. 4(d), we plot the variation of $J_c$ with temperature for J1 and J2. Below 5 K, $J_c$ reaches values in excess of $10^9$ Am$^{-2}$. Interestingly, despite its larger junction length (see Table 1), J2 has a significantly larger critical current density than J1. We believe that this enhancement results from a higher interface transparency due to the use of Ag, which, unlike Cu, does not form oxides at the interface with $CrO_2$. The critical current density for our JJs is an order of magnitude higher than standard S-F-S JJs [17,31], despite the fact that our devices are almost 100 times longer, supporting the notion that exceptionally large triplet supercurrents can be generated in half-metallic ferromagnets. The device lengths are also significantly larger than the typical mean free path of $CrO_2$, which is of the order of 50 nm [15,32]; therefore, our JJs are in the diffusive long junction limit. It has been theoretically predicted that the temperature dependence of the critical current of $CrO_2$-based JJs would exhibit a peak at low temperature, and the position of the peak is determined by the junction length [15]. Since our junction lengths are very long, we expect such a peak to occur at temperatures lower than 2 K, which cannot be achieved in our present measurement setup. At the measured temperatures, we expect $J_c$ to be proportional to $T^{3/2}\exp[(2\pi k_B T/E_{th})^{1/2}]$, where $E_{th}$ is the Thouless energy of the junction [33]. The inset of Fig. 4(d) clearly shows that this is indeed the case for J1, where $\ln(J_c) - 3/2\ln(T)$ varies linearly with $T^{1/2}$. The slope of this plot allows us to directly estimate $E_{th} \sim 11\ \mu$V. Using previous

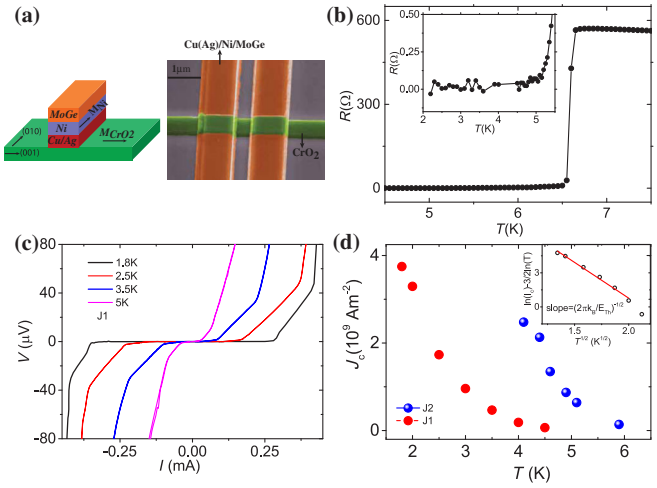


FIG. 4. Josephson junctions with $CrO_2$ wires. (a) Schematic of Josephson junctions fabricated with $CrO_2$ wire as a weak link. We show the scanning electron micrograph (false color) of a Josephson junction on a $CrO_2$ nanowire (green). The graph also shows crystal and magnetization directions. Orange contact pads consist of trilayer (Cu or Ag)/Ni/MoGe. (b) Resistance $R$ versus temperature $T$ for junction J1. The inset shows the behavior around zero resistance. (c) Current $I$ versus voltage $V$ characteristics of J1 at different temperatures. (d) Critical current density $J_c$ versus $T$. The inset shows a linear fit to a plot of $\ln(I_c) - 3/2\ln(T)$ vs $T^{1/2}$.

TABLE I. Wire width, wire thickness, and junction length of two Josephson junction devices based on $CrO_2$ nanowires.

| Device | Width | Thickness | Junction length |
|---|---|---|---|
| J1 (Cu) | 1 $\mu$m | 75 nm | 400 nm |
| J2 (Ag) | 500 nm | 150 nm | 600 nm |

estimates of the diffusion constant $D = 3.7 \times 10^{-3}$ $m^2 s^{-1}$ from a Fermi velocity of $2.2 \times 10^5$ $m s^{-1}$, and a typical mean free path of 50 nm [34], we calculate $E_{th} = \hbar D/L^2$ to be 15 $\mu$V for our junction length of L = 400 nm, in good agreement with our experiments.

In conclusion, we have shown that a detailed understanding of selective area growth of $CrO_2$ allows us to reliably produce high-quality nanowires with a well-defined geometry and magnetization. Proximizing these wires with a superconductor produces S-F-S Josephson junctions that support record-high triplet supercurrents over long distances. The estimated current densities are large enough to envision devices where such spin-polarized supercurrents could be used to manipulate the magnetization of a nanomagnet [1,35]. Furthermore, the use of a patterned growth technique would allow one to engineer domain walls at predefined locations [36,37], thereby realizing a scalable device architecture where fully spin-polarized supercurrents could be used to create spintronic devices without dissipation.

## ACKNOWLEDGMENTS

Technical support from M. B. S. Hesselberth, D. Boltje, and A. F. Beker is gratefully acknowledged. We also strongly benefited from discussions with S. Goswami. This work is part of the research program of the Foundation for Fundamental Research on Matter (FOM), which is part of the Netherlands Organisation for Scientific Research (NWO). The work was also supported by the EU COST action MP1201 "NanoSC" and by a grant from the Leiden-Delft Consortium "NanoFront".

## APPENDIX: METHODS

### 1. Selective area growth

We start with a rutile (100) $TiO_2$ substrate, which has a tetragonal surface net spanned by the $b$- and $c$-crystal axes ($b = 0.459$ nm, $c = 0.296$ nm; note that $a = b$), on which $CrO_2$ ($b = 0.442$ nm, $c = 0.292$ nm) can be grown isostructurally. The lattice mismatch is anisotropic, being $-1.4\%$ along the $b$ axis and $-3.8\%$ along the $c$ axis. This leads to anisotropic growth rates, which are important for nanowire growth. Substrates were cleaned with organic solvents (Acetone/IPA) followed by HF treatment, on which a 25-nm $SiO_x$ thin film was sputter deposited. Using e-beam resist and lithography, openings of different sizes and shapes were created in the resist along different crystallographic directions. $SiO_x$ was selectively removed from the openings using reactive ion etching with a $CF_4$ and an $O_2$ plasma. The etch time of $SiO_x$ is critical because underetching results in only partial removal of $SiO_x$, while overetching damages the underlying $TiO_2$ substrate, which affects the film quality adversely (see Fig. 4 of Ref. [25]). Next, $CrO_2$ was grown selectively in the $SiO_x$ trenches (trench width $w_{tr}$) by CVD in a two-zone furnace, where the substrate temperature was kept at 395 °C, while the precursor $CrO_3$ was heated to 260 °C in the presence of a flow of 100 sccm $O_2$ carrier gas. By monitoring the growth times ($t_g$), samples with varying thicknesses were prepared. Each sample consists of $CrO_2$ structures with different sizes, shapes, aspect ratios, and orientations. SEM, atomic force microscopy, and MFM were used to examine the structural and magnetic morphology of the $CrO_2$ nanostructures. For the MFM measurements, the samples were magnetized in a 1-T field along the easy axis, followed by a decrease of the field to −8 mT in order to create a domain state.

### 2. Fabrication of lateral Josephson junctions.

To fabricate JJs, trilayer [Cu or Ag (5 nm)/Ni (1.5 nm)/MoGe (100 nm)] contact pads, defined by electron beam lithography, were sputter deposited on $CrO_2$ wires, followed by a lift-off process. $CrO_2$ is a metastable phase and inevitably reduces to more stable $Cr_2O_3$, which is antiferromagnetic and insulating. The surface of $CrO_2$ is etched *in situ* with an argon plasma prior to the sputtering of the trilayer contact pads, which are deposited without breaking the vacuum. The optimized etching parameters, in combination with faceted $CrO_2$ crystals, produced JJS with high interface transparency.

[1] S. S. P. Parkin, M. Hayashi, and L. Thomas, *Magnetic Domain-Wall Racetrack Memory*, Science **320**, 190 (2008).
[2] V. E. Demidov, S. Urazhdin, and S. Demokritov, *Direct Observation and Mapping of Spin Waves Emitted by Spin-Torque Nano-Oscillators*, Nat. Mater. **9**, 984 (2010).
[3] J. C. Slonczewski, *Current-Driven Excitation of Magnetic Multilayers*, J. Magn. Magn. Mater. **159**, L1 (1996).
[4] Y. Huai, F. Albert, P. Nguyen, M. Pakala, and T. Valet, *Observation of Spin-Transfer Switching in Deep Submicron-Sized and Low-Resistance Magnetic Tunnel Junctions*, Appl. Phys. Lett. **84**, 3118 (2004).
[5] F. S. Bergeret, A. F. Volkov, and K. B. Efetov, *Long-Range Proximity Effects in Superconductor-Ferromagnet Structures*, Phys. Rev. Lett. **86**, 4096 (2001).
[6] M. Eschrig, J. Kopu, J. C. Cuevas, and G. Schön, *Theory of Half-Metal/Superconductor Heterostructures*, Phys. Rev. Lett. **90**, 137003 (2003).
[7] M. Houzet and A. I. Buzdin, *Long Range Triplet Josephson Effect through a Ferromagnetic Trilayer*, Phys. Rev. B **76**, 060504(R) (2007).
[8] M. S. Anwar, M. Veldhorst, A. Brinkman, and J. Aarts, *Long Range Supercurrents in Ferromagnetic* $CrO_2$ *Using a Multilayer Contact Structure*, Appl. Phys. Lett. **100**, 052602 (2012).
[9] N. Banerjee, J. W. A. Robinson, and M. G. Blamire, *Reversible Control of Spin-Polarized Supercurrents in Ferromagnetic Josephson Junctions*, Nat. Commun. **5**, 4771 (2014).
[10] T. S. Khaire, M. A. Khasawneh, W. P. Pratt, Jr., and N. O. Birge, *Observation of Spin-Triplet Superconductivity in Co-Based Josephson Junctions*, Phys. Rev. Lett. **104**, 137002 (2010).

[11] J. Wang, M. Singh, M. Tian, N. Kumar, B. Liu, C. Shi, J. K. Jain, N. Samarth, T. E. Mallouk, and M. H. W. Chan, *Interplay Between Superconductivity and Ferromagnetism in Crystalline Nanowires*, Nat. Phys. **6**, 389 (2010).

[12] M. Eschrig, *Spin-Polarized Supercurrents for Spintronics: A Review of Current Progress*, Rep. Prog. Phys. **78**, 104501 (2015).

[13] J. Linder and J. W. A. Robinson, *Superconducting Spintronics*, Nat. Phys. **11**, 307 (2015).

[14] N. G. Pugach and A. I. Buzdin, *Magnetic Moment Manipulation by Triplet Josephson Current*, Appl. Phys. Lett. **101**, 242602 (2012).

[15] M. Eschrig and T. Lofwander, *Triplet Supercurrents in Clean and Disordered Half-Metallic Ferromagnets*, Nat. Phys. **4**, 138 (2008).

[16] E. C. Gingrich, P. Quarterman, Yixing Wang, R. Loloee, W. P. Pratt, Jr., and N. O. Birge, *Spin-Triplet Supercurrent in* Co/Ni *Multilayer Josephson Junctions with Perpendicular Anisotropy*, Phys. Rev. B **86**, 224506 (2012).

[17] J. W. A. Robinson, J. D. S. Witt, and M. G. Blamire, *Controlled Injection of Spin-Triplet Supercurrents into a Strong Ferromagnet*, Science **329**, 59 (2010).

[18] S. Mironov and A. Buzdin, *Triplet Proximity Effect in Superconducting Heterostructures with a Half-Metallic Layer*, Phys. Rev. B **92**, 184506 (2015).

[19] R. S. Keizer, S. T. B. Goennenwein, T. M. Klapwijk, G. X. Miao, G. Xiao, and A. Gupta, *A Spin Triplet Supercurrent through the Half-Metallic Ferromagnet* $CrO_2$, Nature (London) **439**, 825 (2006).

[20] M. S. Anwar, F. Czeschka, M. Hesselberth, M. Porcu, and J. Aarts, *Long-Range Supercurrents through Half-Metallic Ferromagnetic* $CrO_2$, Phys. Rev. B **82**, 100501 (2010).

[21] A. Singh, S. Voltan, K. Lahabi, and J. Aarts, *Colossal Proximity Effect in a Superconducting Triplet Spin Valve Based on the Half-Metallic Ferromagnet* $CrO_2$, Phys. Rev. X **5**, 021019 (2015).

[22] X. L. Wang, A. Di Bernardo, N. Banerjee, A. Wells, F. S. Bergeret, M. G. Blamire, and J. W. A. Robinson, *Giant Triplet Proximity Effect in Superconducting Pseudo Spin Valves with Engineered Anisotropy*, Phys. Rev. B **89**, 140508(R) (2014).

[23] P. G. Ivanov, S. M. Watts, and D. M. Lind, *Epitaxial Growth of* $CrO_2$ *Thin Films by Chemical-Vapor Deposition from a* $Cr_8O_{21}$ *Precursor*, J. Appl. Phys. **89**, 1035 (2001).

[24] H. A. Bullen and S. J. Garrett, *Epitaxial Growth of* $CrO_2$ *Thin Films on* $TiO_2$ *(110) Surfaces*, Chem. Mater. **14**, 243 (2002).

[25] See Supplemental Material at http://link.aps.org/supplemental/10.1103/PhysRevX.6.041012 for details of pendeoepitaxy growth and the correlation between vertical and lateral overgrowth.

[26] X. Zou and G. Xiao, *Magnetic Domain Configurations of Epitaxial Chromium Dioxide (*$CrO_2$*) Nanostructures*, Appl. Phys. Lett. **91**, 113512 (2007).

[27] A. Tanaka, R. Chen, K. L. Jungjohann, and S. A. Dayeh, *Strong Geometrical Effects in Submillimeter Selective Area Growth and Light Extraction of GaN Light Emitting Diodes on Sapphire*, Sci. Rep. **5**, 17314 (2015).

[28] A. Gupta, X. W. Li, S. Guha, and G. Xiao, *Selective-Area and Lateral Overgrowth of Chromium Dioxide (*$CrO_2$*) Films by Chemical Vapor Deposition*, Appl. Phys. Lett. **75**, 2996 (1999).

[29] C. König, M. Fonin, M. Laufenberg, A. Biehler, W. Bührer, M. Kläui, U. Rüdiger, and G. Güntherodt, *Micromagnetism and Magnetotransport Properties of Micron-Sized Epitaxial* $CrO_2$ *(100) Wires*, Phys. Rev. B **75**, 144428 (2007).

[30] A. Biehler, M. Kläui, M. Fonin, C. König, G. Güntherodt, and U. Rüdiger, *Micromagnetism and Magnetotransport Properties of Micron-Sized Epitaxial* $CrO_2$ *(100) Wires*, Phys. Rev. B **75**, 184427 (2007).

[31] W. M. Martinez, W. P. Pratt, and N. O. Birge, *Amplitude Control of the Spin-Triplet Supercurrent in* $S/F/S$ *Josephson Junctions*, Phys. Rev. Lett. **116**, 077001 (2016).

[32] M. S. Anwar and J. Aarts, *Anomalous Transport in Half-Metallic Ferromagnetic* $CrO_2$, Phys. Rev. B **88**, 085123 (2013).

[33] P. Dubos, H. Courtois, B. Pannetier, F. K. Wilhelm, A. D. Zaikin, and G. Schön, *Josephson Critical Current in a Long Mesoscopic S-N-S Junction*, Phys. Rev. B **63**, 064502 (2001).

[34] S. P. Lewis, P. B. Allen, and T. Sazaki, *Band Structure and Transport Properties of* $CrO_2$, Phys. Rev. B **55**, 10253 (1997).

[35] T. Koyama, D. Chiba, K. Ueda, K. Kondou, H. Tanigawa, S. Fukami, T. Suzuki, N. Ohshima, N. Ishiwata, Y. Nakatani, K. Kobayashi, and T. Ono, *Observation of the Intrinsic Pinning of a Magnetic Domain Wall in a Ferromagnetic Nanowire*, Nat. Mater. **10**, 194 (2011).

[36] M. Kläui, C. A. F. Vaz, J. A. C. Bland, L. J. Heyderman, F. Nolting, A. Pavlovska, E. Bauer, S. Cherifi, S. Heun, and A. Locatelli, *Head-to-Head Domain-Wall Phase Diagram in Mesoscopic Ring Magnets*, Appl. Phys. Lett. **85**, 5637 (2004).

[37] A. Wachowiak, J. Wiebe, M. Bode, O. Pietzsch, M. Morgenstern, and R. Wiesendanger, *Direct Observation of Internal Spin Structure of Magnetic Vortex Cores*, Science **298**, 577 (2002).